RESEARCH ARTICLE

Editor's Choice

ADVANCED MATERIALS
www.advmat.de

In Vivo Microrheology Reveals Local Elastic and Plastic Responses Inside 3D Bacterial Biofilms

Takuya Ohmura, Dominic J. Skinner, Konstantin Neuhaus, Gary P. T. Choi, Jörn Dunkel, and Knut Drescher**

Bacterial biofilms are highly abundant 3D living materials capable of performing complex biomechanical and biochemical functions, including programmable growth, self-repair, filtration, and bioproduction. Methods to measure internal mechanical properties of biofilms in vivo with spatial resolution on the cellular scale have been lacking. Here, thousands of cells are tracked inside living 3D biofilms of the bacterium *Vibrio cholerae* during and after the application of shear stress, for a wide range of stress amplitudes, periods, and biofilm sizes, which revealed anisotropic elastic and plastic responses of both cell displacements and cell reorientations. Using cellular tracking to infer parameters of a general mechanical model, spatially-resolved measurements of the elastic modulus inside the biofilm are obtained, which correlate with the spatial distribution of the polysaccharides within the biofilm matrix. The noninvasive microrheology and force-inference approach introduced here provides a general framework for studying mechanical properties with high spatial resolution in living materials.

1. Introduction

Bacterial biofilm communities are estimated to be the most abundant biomaterial on Earth[1] and play important roles in human health, from the gut microbiome to infections.[2–4] In bioengineering and materials science, biofilms are currently intensely studied as a prototypical class of programmable multifunctional living materials[5,6] that integrate mechanical robustness and adaptivity with self-repair and chemical synthesis capabilities.[7,8] Although biofilms are materials with broad technological potential, bacterial biofilms can also be a problem in medical settings and industrial pipes, as they are highly resilient to antibiotics, disinfectants, and mechanical stresses.[2–4,9–11] Consequently, controlling biofilm growth and mechanical properties are important challenges for technological applications and for removing unwanted biofilms in infections and industry.

Biofilms are typically 3D structures that grow on surfaces, either by consuming nutrients within the surface, or by consuming nutrients in the aqueous phase above the surface. Within bacterial biofilms, cells are attached to each other and to the surface with a self-produced extracellular matrix comprising proteins, nucleic acids, polysaccharides, and lipids, which together form a complex mechanically resilient material structure.[5,12–15] The exact molecular composition of the matrix varies between biofilms of different bacterial species.[15] The industrial and medical significance of biofilm removal[2–4,9–11] led to several studies of the global material properties of whole biofilms at macroscopic scales (100 μm–10 cm),[16–29] identifying important roles for particular matrix components.[30–32] Depending on the global material properties of biofilms, strong fluid flow has been shown to significantly deform the shape of biofilms,[18–21,33] including the formation of biofilm streamers for bacterial species that produce viscoelastic biofilms.[34–39]

While important insights have been obtained for the global material properties of whole biofilms, much less is known about the spatial distributions of material properties within biofilms and their consequences. Spatially resolved measurements of gene expression in biofilms revealed that there is significant physiological heterogeneity at the cellular length scale.[40–42] Furthermore, the matrix composition inside biofilms also varies on the cellular length scale.[43–47] Mechanical properties likely

T. Ohmura, K. Neuhaus, K. Drescher
Biozentrum
University of Basel
Spitalstrasse 41, Basel 4056, Switzerland
E-mail: knut.drescher@unibas.ch

D. J. Skinner, J. Dunkel
Department of Mathematics
Massachusetts Institute of Technology
77 Massachusetts Avenue, Cambridge, MA 02139-4307, USA
E-mail: dunkel@mit.edu

D. J. Skinner
NSF-Simons Center for Quantitative Biology
Northwestern University
Evanston, IL 60201, USA

K. Neuhaus
Department of Physics
Philipps-Universität Marburg
Renthof 5, 35032 Marburg, Germany

G. P. T. Choi
Department of Mathematics
The Chinese University of Hong Kong
N.T. Hong Kong

The ORCID identification number(s) for the author(s) of this article can be found under https://doi.org/10.1002/adma.202314059

DOI: 10.1002/adma.202314059

also vary on the cellular length scale in biofilms, yet the relationship between the spatial distribution of matrix components and local material properties on these microscopic scales remains unknown.

To investigate material properties with spatial resolution inside biofilms, previous studies have inserted microscopic beads inside biofilms. The beads' passive diffusion or displacements following active perturbations can be used to infer the mechanical environment around the beads.[28,48–51] In contrast to microbeads that are placed inside biofilms, bacterial cells are anchored to the extracellular biofilm matrix and to each other through self-produced proteins and polysaccharides on their cell surface.[13,46] Therefore, bacterial cells are likely to be more accurate tracers for the local material properties inside biofilms than microbeads.[27] Based on this concept, we sought to measure the local mechanical properties of 3D bacterial biofilms noninvasively at cellular resolution. To achieve this, we coupled highly reproducible microfluidic biofilm cultivation systems and flow control[52] with recent advances in 3D live-cell microscopy and highly-accurate deep-learning-based image analysis for cell detection.[53–56]

Our experimental platform enabled us to track the individual cells in 3D biofilms of *Vibrio cholerae* during and after exposure to strong fluid shear, for a wide range of different shear rate amplitudes, exposure periods, and biofilm sizes. To reconstruct the internal material properties of biofilms, we developed a computational inference method for estimating elastic forces from cell tracking data. Based on the experimental cell coordinate changes, we were also able to quantify the plasticity inside biofilms at cellular resolution, which is defined as the difference in biofilm architecture before and after the exposure to fluid shear, as determined by changes in cell positions and orientations. Our measurements revealed a correlation between the spatial distribution of mechanical stiffness and the spatial distribution of particular a molecular component of the extracellular matrix in biofilms. Beyond providing a finely resolved picture of the local elasto-plastic stress response inside bacterial biofilms, the integrated experimental and computational methods developed here can provide a foundation for the noninvasive rheological analysis of biological material at cell-level resolution.

2. Results and Discussion

2.1. Strong Shear Flow Induces Spatially Distributed Elastic and Plastic Responses in Bacterial Biofilms

To study the mechanical properties of biofilms, we grew *V. cholerae* biofilms in microfluidic channels from a single cell up to a community size in the range of 521–9554 cells, where the largest cell numbers correspond to biofilm colonies with approximately hemispherical shape and a 50 μm diameter, 17 μm height, and volume of 5246 μm^3. During biofilm cultivation, cells were exposed to a constant flow of minimal M9 medium at a very low shear rate ($\dot{\gamma} = 20.4\ s^{-1}$ at the bottom surface of the channel), which are environmental conditions that resulted in a median cell volume of 0.5 μm^3 inside biofilms. We then stopped the flow and performed the following experiment (**Figure 1**A, see also Video S1, Supporting Information): We acquired a 3D high-resolution image of all cells in the biofilm, followed by increasing the flow rate through the microfluidic channel to obtain a shear rate of $\dot{\gamma} = 8.16 \times 10^4\ s^{-1}$ (average flow speed in the channel: $u_{average} = 0.95\ m\ s^{-1}$), and we then acquired another 3D image. After applying this strong shear rate for a particular duration (3–40 min), we stopped the flow again, and acquired a final 3D high-resolution image of the biofilm.

Using bacterial single-cell segmentation and an iterative tracking algorithm involving the computation of strain fields (Figure 1B), which was developed specifically for the image datasets generated by our experiments (see the Experimental Section; and Figure S1, Supporting Information), we tracked cells in 274 independent biofilms across all three time points. Based on these cell tracks, we computed the cell displacements during the biofilm deformation caused by increasing the shear rate from 0 to $8.16 \times 10^4\ s^{-1}$ (Figure 1C), and during the biofilm recovery caused by reducing the shear rate from 8.16×10^4 to $0\ s^{-1}$ (Figure 1D). By comparing the positions of cells after biofilm recovery with their initial positions, we were able to investigate and quantify the local biofilm plasticity (Figure 1E). During recovery, the cell displacements are similar in magnitude (but opposite in direction) to the cell displacements during deformation, resulting in a biofilm shape after the flow decrease that appears similar to the biofilm shape before the flow increase. However, during deformation and recovery, some of the outermost cells have been ripped off, and there is a net cell displacement of the cells that remained attached. Together, these results indicate that the biofilm displays a large elastic response, with a smaller plastic component (Figure 1C–E).

To quantify the spatial distribution of biofilm architecture changes for biofilm deformation, recovery, and plasticity, we measured two additional cell displacement-related parameters, and two parameters related to the changes in cellular orientation: We measured the length of cell displacement $\Delta r_{ij} = |\boldsymbol{r}_i - \boldsymbol{r}_j|$ and the y-component of the angular-momentum-like cross product $\boldsymbol{r}_i \times \Delta\boldsymbol{r}_{ij}$ (see **Figure 2**A for definitions of variables), and we measured the local nematic order parameter $S_k = \langle \frac{3}{2}(\boldsymbol{n}_k \cdot \boldsymbol{n}_l)^2 - \frac{1}{2} \rangle_{l \in L}$, as well as the angle $\theta_z = \text{acos}(\boldsymbol{n}_k \cdot \boldsymbol{e}_z)$ between the cell's major axis $\boldsymbol{n}_k$ and the z-axis (see Figure 2B for definitions of geometry and variables).

The cell displacement field Δr for biofilm deformation, recovery, and plasticity revealed that displacement magnitudes increased along the z-axis (Figure 2C), which correlates with the increase of the flow speed u_x for higher z-positions, ranging from $u_x = 0\ \mu m\ s^{-1}$ at the bottom of the biofilm to $u_x = 1.43\ m\ s^{-1}$ at the top of the biofilm, corresponding to a shear rate of $\dot{\gamma} = 8.16 \times 10^4\ s^{-1}$ at the bottom surface of the channel (for a flow rate of 2000 μL min^{-1}, see the Experimental Section). Despite the high flow speed, the flow field in our microfluidic channel is laminar, with a parabolic profile that is consistent with predictions from fluid mechanics theory (Figure S2 and Video S2, Supporting Information). The direction of the cell displacements in the xz-plane revealed a rotation of the biofilm around the y-axis at $(x,z) = (0,0)$ (Figure 1C–E, see also individual displacement coordinates in Figure S3A, Supporting Information), reminiscent of solid body rotation. The y-component of the displacement cross product $(\boldsymbol{r}_i \times \Delta\boldsymbol{r}_{ij})_y$ is largest toward the fluid-facing surfaces of the biofilm which experience fluid shear, in a pattern that is consistent with solid body rotation (Figure 2C). The cell displacements in the xy-plane revealed that the biofilm expands in the y-direction during deformation (Figure S3B, Supporting

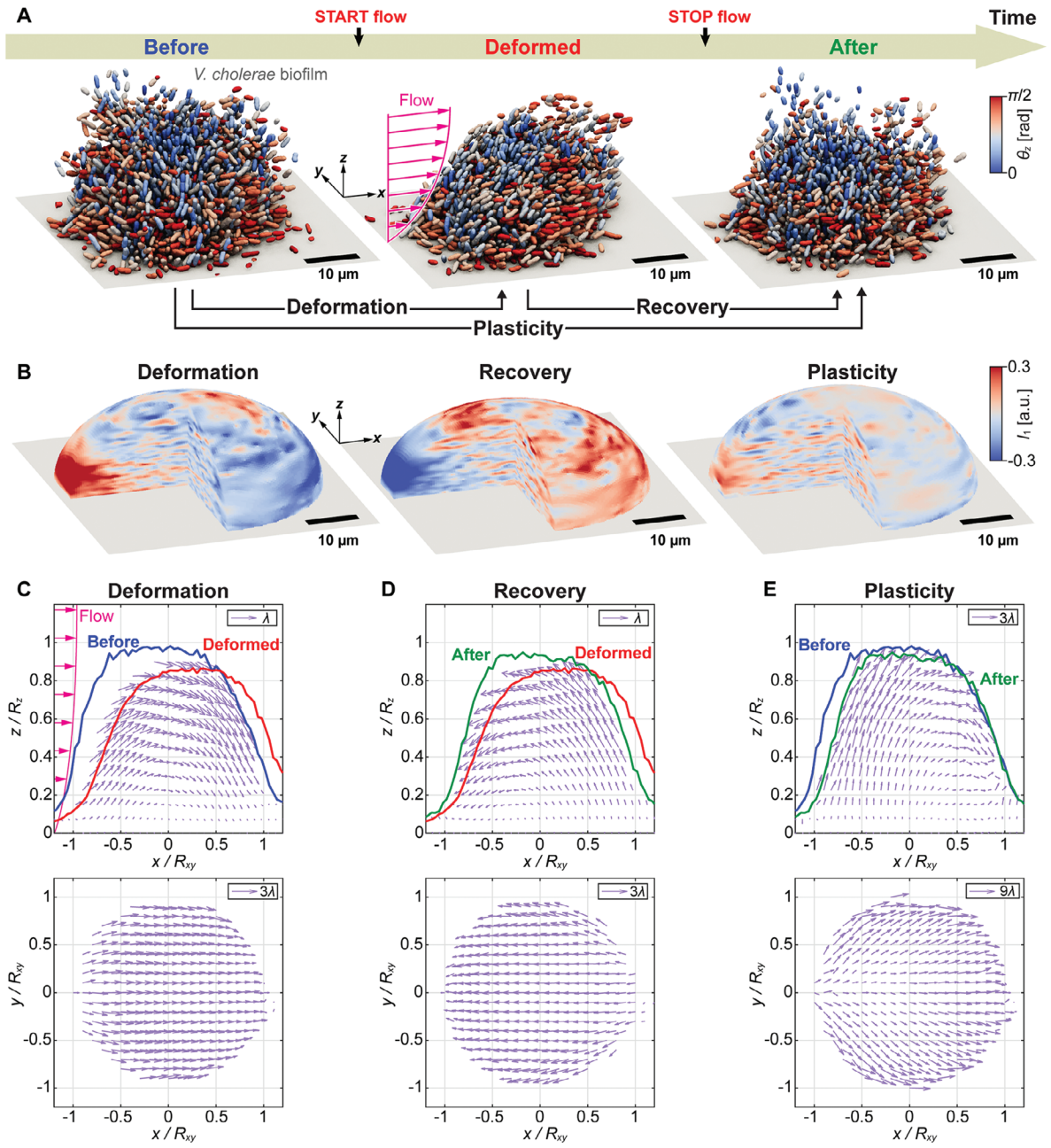

Figure 1. Biofilm deformation, recovery, and plasticity caused by changes in shear flow. A) A *V. cholerae* biofilm colony (5013 cells, $V = 3891\ \mu m^3$) attached to a glass surface in a microfluidic channel was 3D-imaged at single-cell level to track the architectural changes caused by the application of strong shear flow (shear rate $\dot{\gamma} = 8.16 \times 10^4\ s^{-1}$). Cells are colored according to their angle with the *z*-axis. The first 3D-image time point, termed "Before," was acquired without flow through the channel. After acquiring the first 3D image, the flow rate was increased from 0 to 2000 μL min^{-1} and held constant for a certain duration (3–40 min). The second 3D-image time point, termed "Deformed," was acquired 1 min into the application of strong flow along the *x*-axis. The third 3D-image time point, termed "After" was acquired 1 min after the strong flow was stopped again. In this study, we refer to biofilm architecture changes between the first two time points as "Deformation," between the last two time points as "Recovery," and between the first and last time point as "Plasticity." B) Strain field magnitudes ($I_1 = \epsilon_{xx} + \epsilon_{yy} + \epsilon_{zz}$) for biofilm deformation (left), recovery (middle), and plasticity (right) were computed based on a 3D quasiconformal mapping between two time points, using the cell centroid coordinates. The average result from $n = 9$ independent replicate biofilms is shown on a hemi-ellipsoidal domain, with one quarter removed for visualization of the interior. C) Biofilm deformation, visualized in the *xz*-plane (top) and the *xy*-plane (bottom): Vector fields of averaged cell displacements caused by an increase in fluid shear rate from 0 to $8.16 \times 10^4\ s^{-1}$. For the *xy*-plane vector field, cell displacements at all *z*-coordinates are included in the average. For the *xz*-plane vector field, cell displacements at all *y*-coordinates are included in the average. D) Biofilm recovery, visualized in the *xz*-plane (top) and the *xy*-plane (bottom): Vector fields of averaged cell displacements after reducing the fluid shear rate from 8.16×10^4 to $0\ s^{-1}$. E) Biofilm plasticity, visualized in the *xz*-plane (top) and the *xy*-plane (bottom): Vector fields of averaged cell displacements. In panels (C–E) the unit of the displacement vector λ is consistent across all plots, but scaled as shown in the inset of each plot. For panels (C–E), data from $n = 87$ independent replicate biofilms were used, by first normalizing the size of each biofilm by the radius *R*, followed by averaging the cell displacement in spatial bins of size 0.05 x *R*, across all biofilms.

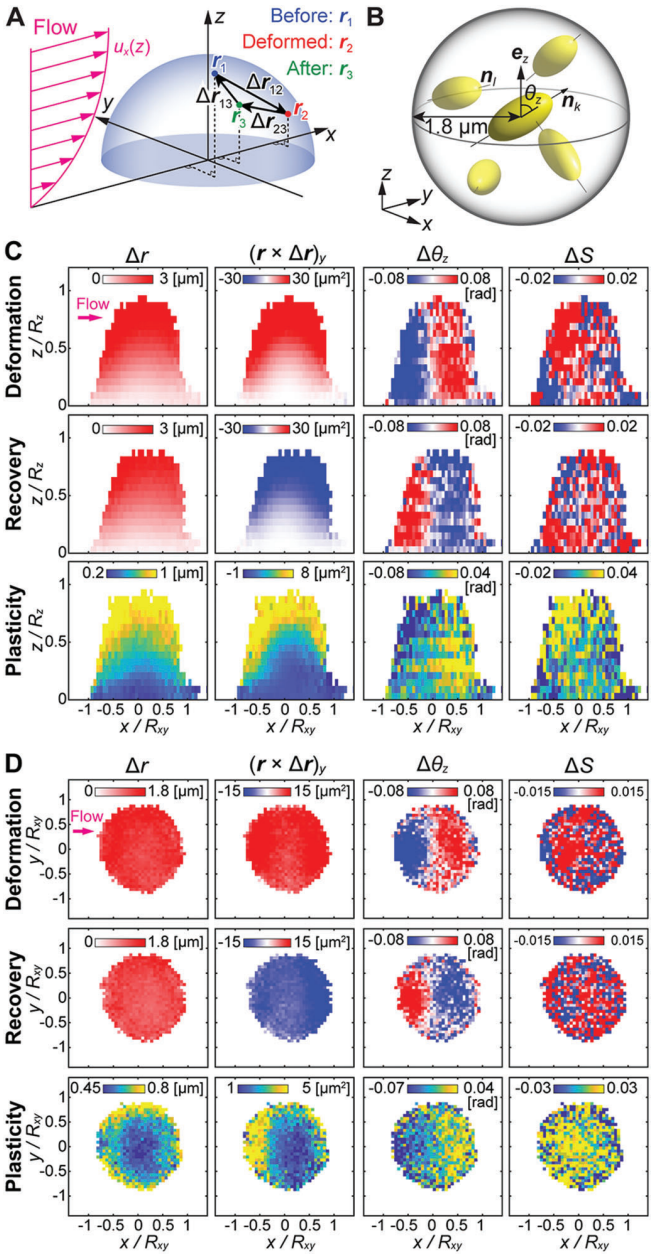

Figure 2. Biofilm architecture changes at the cellular level during deformation, recovery, and plasticity. A) Schematic illustration for coordinates in this study: Flow is along the *x*-axis; gray hemisphere indicates biofilm shape; cell centroid *xyz*-coordinates before, during, and after flow are described as r_1, r_2, and r_3, respectively. B) Schematic illustration for definitions of θ_z and the unit vector n along a cell's major axis, used in the definition of the local nematic order parameter S_k, which was computed for all cells with index $l \in L$ that are located within 1.8 µm from the cell surface of the focal cell with index k. C) Side-view (*xz*-plane) of biofilm deformation, recovery, plasticity for four single-cell-level architectural parameters (Δr, displacement; $(r \times \Delta r)_y$, *y*-component of the angular-momentum-like displacement cross product; $\Delta\theta_z$, change in angle of the cell major axis with the *z*-axis; ΔS, change in the local nematic order parameter). D) Top-view (*xy*-plane) of biofilm deformation, recovery, plasticity for four architectural parameters (Δr, $r \times \Delta r$, $\Delta\theta_z$, ΔS). In panels (C) and (D), the changes in biofilm architecture were measured for $n = 13$ independent biofilms with volume $V > 2800$ µm^3, exposed to a shear rate $\dot{\gamma} = 8.16 \times 10^4$ s^{-1} for a duration of 20 or 40 min.

Information), which is a change that is not retraced during the recovery period, leading to a net plastic expansion of the biofilm in the *y*-direction (Figure S3B (Supporting Information); and Figure 1E), and an overall plastic reduction in cell number density ρ_{Number} (Figure S3A,B, Supporting Information).

Cell orientation changes during biofilm deformation (Figure 2C,D) show that $\Delta\theta_z < 0$ in the upstream part of the biofilm, indicating that cells become more vertically aligned in this region, whereas $\Delta\theta_z > 0$ in the downstream part of the biofilm, indicating that cells are reoriented toward the *xy*-plane in this region. These cell orientation changes during biofilm deformation are partially retraced during recovery, yet a significant plastic change in cell orientation $\Delta\theta_z$ remains after the flow is stopped again (Figure 2C,D). Interestingly, the changes in local nematic order parameter, ΔS, are similar in magnitude across deformation, recovery, and plasticity, displaying a noisy but detectable spatial pattern with the strongest ΔS in the upper region of the upstream part of the biofilm (Figure 2C).

In summary, the measurements of the single-cell-level biofilm architecture parameters revealed that plastic cell displacements are largest in locations where the deformation and recovery cell displacements are also largest. However, plastic cell displacements are relatively small compared with the deformation and recovery cell displacements. In contrast, the plastic changes in cell orientation and nematic order parameter are of similar magnitude to the changes of these parameters during deformation and recovery.

2.2. Biofilm Size, Fluid Shear, and Duration of Shear Exposure Influence Elastic and Plastic Changes of Biofilm Architecture

To determine which properties of our system influence the magnitude of the biofilm architecture changes, we performed similar measurements with biofilms of different volume, for different maximum shear rates, and for different durations of exposure to the maximum shear rate. For each of these experiments, we then computed Δr, $|(\boldsymbol{r} \times \Delta \boldsymbol{r})_y|$, $|\Delta S|$, and $|\Delta\theta_z|$, as average values for all cell tracks in all replicate biofilms. These experiments showed that large shear rates and large biofilm volumes generally result in higher cell displacement parameters (Δr, $|(\boldsymbol{r} \times \Delta \boldsymbol{r})_y|$) for biofilm deformation (**Figure 3**A), recovery (Figure 3B), and plasticity (Figure 3C), except for the Δr plasticity, which did not strongly depend on the biofilm volume. Interestingly, these experiments also showed that the largest change in cell orientation ($|\Delta S|$, $|\Delta\theta_z|$) occurs for small biofilm volumes and large shear rates (Figure 3). Small biofilms exhibit strong changes in cell orientation, because the surface-to-volume ratio is large and a larger fraction of cells directly experience the fluid shear. However, biofilms with small volume do not exhibit large cell displacements, because their height is relatively low and cellular *z*-position is the key determinant for cell displacements (Figures 1C–E and 2C). For each of the four parameters (Δr, $|(\boldsymbol{r} \times \Delta \boldsymbol{r})_y|$, $|\Delta S|$, $|\Delta\theta_z|$), the patterns of the biofilm volume versus shear rate heatmaps are similar across deformation (Figure 3A), recovery (Figure 3B), and plasticity (Figure 3C). Irrespective of the biofilm volume, the value of the maximum shear rate is a key control parameter for the magnitude of the architectural changes during deformation, recovery, and plasticity (Figure 3).

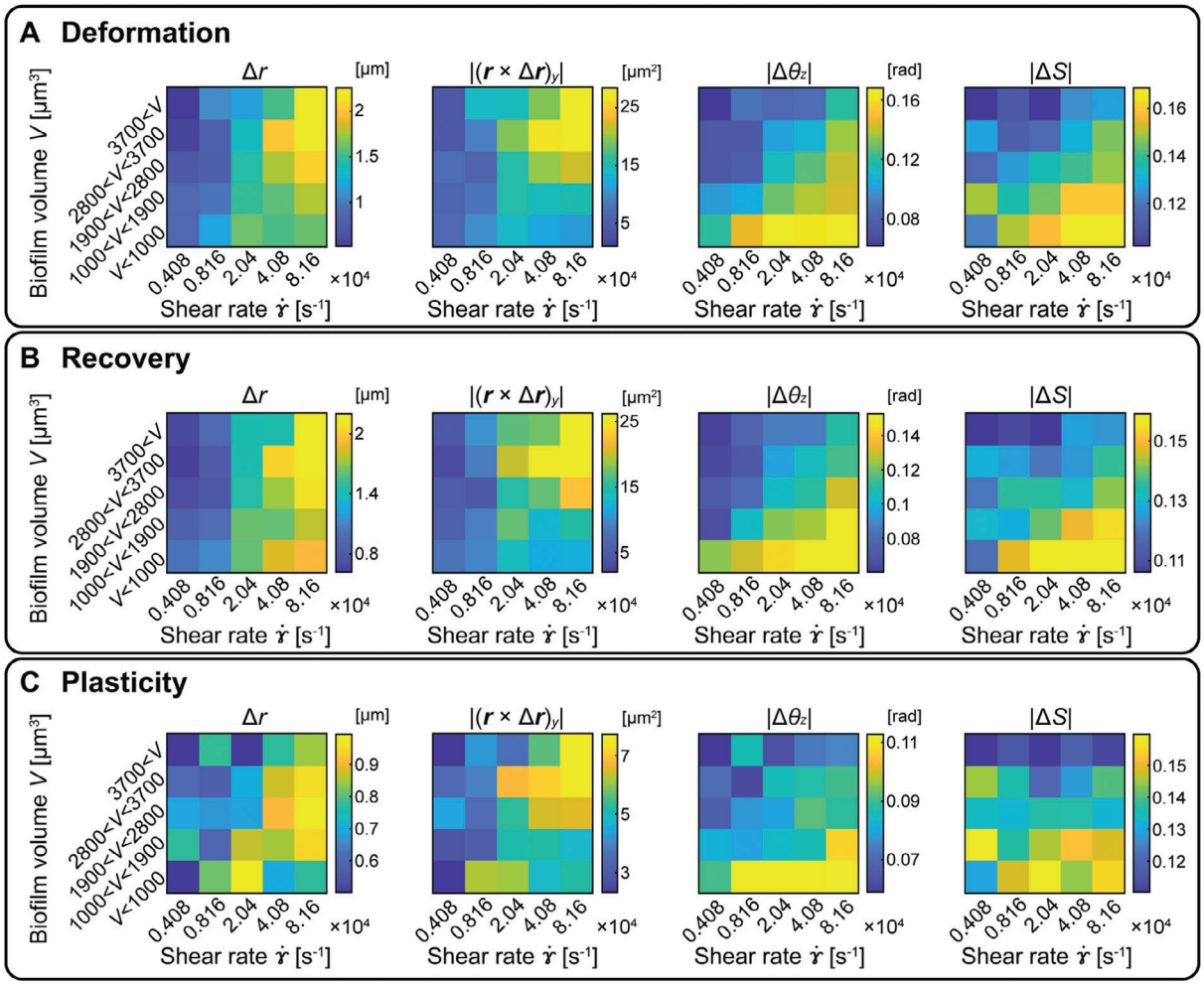

Figure 3. Phase diagrams showing the influence of maximum flow rate and biofilm volume on architectural changes during biofilm deformation, recovery, and plasticity. A) Biofilm architecture changes during deformation. Each heatmap shows the effect of the maximum flow rate and the biofilm volume V on the biofilm architecture parameters (Δr, cell displacement; $|(r \times \Delta r)_y|$, angular-momentum-like displacement cross-product; $|\Delta\theta_z|$, change in cell alignment with the z-axis; $|\Delta S|$, change in local nematic order). Each pixel within a heatmap is the average value for all cells in all biofilms in this condition. B) Biofilm architecture changes during recovery (after reducing the shear rate from its maximum value back to 0 s^{-1}). C) Biofilm architecture changes characterizing plasticity. For each pixel in every heatmap, data from $n \geq 3$ independent replicate biofilms were averaged.

Varying the duration of the biofilm exposure to the maximum shear rate from 3 to 40 min does not systematically change the cell displacement metrics for biofilm deformation and recovery, but longer durations do result in higher plasticity of the cell orientation parameters $|\Delta S|$ and $|\Delta\theta_z|$ (see Figure S5 for data of shear rate vs duration, and Figure S6 for data of biofilm volume vs duration, Supporting Information). The fact that the duration of exposure to high flow only affects biofilm plasticity, and not deformation or recovery, suggests that the molecular structure of the matrix either continuously rearranges or bonds within the matrix continuously break during exposure to high shear.

2.3. Spatial Distribution of Elastic Modulus in Biofilms

The biofilm architecture changes during deformation and recovery were similar in magnitude but opposite in direction, indicating an elastic component of the biofilm response to shear flow (Figures 1C–E and 2C,D). To infer the spatial distribution of the elastic modulus within biofilms, we used the spatially-resolved measurements of cell displacements together with a general mechanical model of the biofilm which has the elastic modulus as a parameter. For this model, we created a 3D Delaunay tessellation based on the experimentally-determined cell centroid coordinates of each cell before we apply flow, and we assumed that all neighboring cell centroids i and j that are connected by an edge $e = (i, j)$ in the tessellation are connected by a spring of unknown stiffness k_e, with a rest length l_e^0 (**Figure 4A**, see the Experimental Section). During strong shear flow, the biofilm deforms and we used our experimental cell tracking data to measure the resulting length of each spring l_e. The elastic energy of the system is $H = \sum_e k_e (l_e - l_e^0)^2$, and for each cell i at coordinate $\mathbf{r}_i$ within the interior of the biofilm, the elastic forces balance so that $\partial H / \partial \mathbf{r}_i = 0$. Importantly, elastic forces only balance for cells within the elastic interior of the biofilm, not for

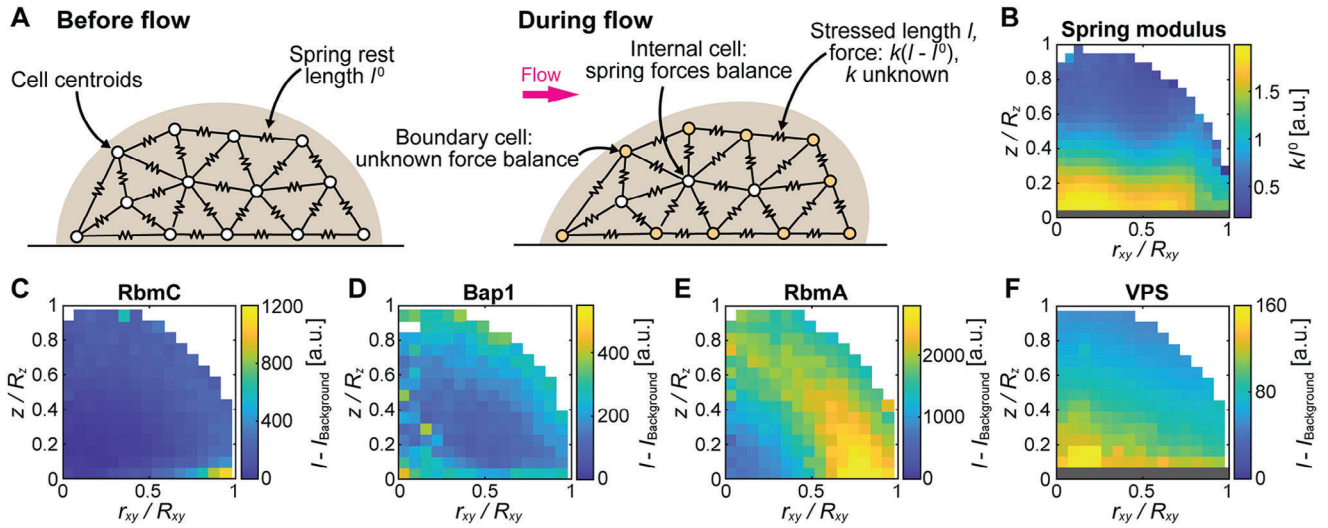

Figure 4. Spatial distribution of material properties in biofilms correlates with spatial distribution of extracellular matrix components. A) Schematic diagram of the model used to infer the spatial distribution of mechanical properties: In this model, the cells centroids that are neighbors in the Delaunay tessellation are connected by a spring of unknown stiffness k, with a rest length l^0. We then used experimental measurements of cell positions before flow and during flow, together with force balance conditions on biofilm-internal cells, to infer the spatial distribution of the relative spring modulus inside the biofilm, without explicitly modeling fluid-to-cell or cell-to-substrate-surface interactions for cells that are part of the biofilm boundary (see the Experimental Section). B) Spatial distribution of spring modulus kl^0 with normalized xy-radial position and normalized z-position. The data are averaged for $n = 10$ independent replicate biofilms. The gray area at the bottom of the heatmap indicates the region occupied by cells that are directly attached to the substrate surface ($0 \leq z/R_z \leq 0.0453$), for which our model cannot provide the spring modulus. C) Spatial distribution of the matrix protein RbmC inside the biofilm, measured using immunofluorescence and confocal microscopy. Additional data for RbmC are shown in Figure S11A (Supporting Information). Data are plotted using the same coordinate system as in panel (B). D) Spatial distribution of the matrix protein Bap1, measured using immunofluorescence. Additional data for Bap1 are shown in Figure S11B (Supporting Information). E) Spatial distribution of the matrix protein RbmA, measured using immunofluorescence. Additional data for RbmA are shown in Figure S11C (Supporting Information). F) Spatial distribution of the matrix polysaccharide VPS, measured using fluorescently conjugated lectins. As shown in the raw images of VPS labeling in Figure S12 (Supporting Information), the lectins preferentially attach to the glass surface, even in regions where no cells are attached. This signal from the glass surface leaks into the higher regions of the biofilm so that we cannot accurately determine the VPS abundance in the gray region. Data for each matrix component was averaged for ≥ 3 independent replicate biofilms. The color scale for each matrix component is the background-subtracted fluorescence intensity.

cells that are part of the boundary of the biofilm (see the Experimental Section), which experience fluid shear forces or cell-to-substrate-surface adhesion forces. Explicitly modeling these external forces for the cells on the boundary of the biofilm is not required to infer biofilm-internal elastic properties. We then solved this model for the spatial distribution of the elastic modulus $l_e^0 k_e$ in biofilms, only searching for solutions which vary continuously (see the Experimental Section). We demonstrated the robustness of this framework by showing that it can accurately recover the spring stiffnesses (k_e) and moduli($l_e^0 k_e$) that we specified in simulated biofilms based on experimentally determined cell centroid positions (Figure S10, Supporting Information).

For the experimental biofilms that experienced strong shear flow (2000 µL min^{-1}), this model revealed a spatial distribution of the elastic modulus that gradually varied across the biofilm (Figure 4B), the biofilms are softest in the outer fluid-facing region of the biofilm, and their elastic modulus increases 12x toward the center of the biofilm.

2.4. Spatial Distribution of Extracellular Matrix Components Accounts for the Elastic Modulus

We hypothesized that the spatial pattern of the spring modulus is caused by variations in the composition of the self-produced extracellular biofilm matrix. To test this, we measured the localization and abundance of the major matrix components of *V. cholerae* biofilms: the proteins RbmA, RbmC, Bap1, and the *Vibrio* polysaccharide (VPS). To directly image the matrix components using confocal microscopy, we used antibodies conjugated with a fluorescent dye for RbmA, RbmC, and Bap1, as well as lectins conjugated with a fluorescent dye for VPS.

These experiments show that for the biofilms in our microfluidic system, RbmC is abundant near the bottom edge of the biofilm (Figure 4C; and Figure S11A, Supporting Information), Bap1 localizes near the bottom surface and the fluid-exposed outer edge of the biofilm (Figure 4D; and Figure S11B, Supporting Information), and RbmA is highly abundant in the region near the fluid-facing surface of the biofilm (Figure 4E; and Figure S11C, Supporting Information). Biofilms formed by mutants that lack RbmC or Bap1 are remarkably resilient to high shear rates, similar to the wild type (Figure S13, Supporting Information). Biofilms without RbmA are easily ripped off the surface by high shear rates (Figure S13, Supporting Information), indicating that this protein is important for the mechanical cohesion of biofilms, as reported in previous studies,[30,46,52,57] likely due to crosslinking the long-chain polysaccharide VPS.[46] However, the spatial distributions of the matrix proteins RbmC, Bap1, and RbmA do not qualitatively correlate with the spatial distribution of the elastic modulus. In contrast, the extracellular matrix

polysaccharide VPS displayed a spatial distribution that closely correlates with the elastic modulus (Figure 4F; and Figure S12, Supporting Information), indicating that VPS abundance is the key factor in determining the elastic cell-cell interactions and the global elastic response of biofilms to shear flow.

3. Conclusion

By subjecting 3D *V. cholerae* biofilms to an increase and decrease in shear flow and by tracking the resulting individual cell displacements and cell reorientations, we were able to perform spatially-resolved in vivo rheological measurements. Despite the strong shear rate ($\dot{\gamma} = 8.16 \times 10^4$ s^{-1}) and shear stress ($\tau = 69.7$ N m^{-2}), corresponding to flow speeds of $u_{\text{average}} = 0.952$ m s^{-1} in the microfluidic channel, the biofilms remained remarkably resilient to the increase in shear flow. The cell displacement tracks within biofilms revealed an elastic response, and a plastic response with a magnitude of ≈1/3 of the elastic response. The cell orientations also revealed a plastic response with a similar magnitude to the elastic response. Furthermore, the elastic and plastic responses were spatially heterogeneous within the biofilms.

The spatial variations in elastic responses within 3D biofilms led us to speculate that the elastic modulus also varies spatially inside these communities. By assuming a general mechanical model for the biofilm based on a network of springs that connect neighboring cells, we used our cell displacement tracks to obtain a spatially resolved map of the spring modulus for cell–cell interactions in biofilms. The spatial distribution of the spring modulus correlates closely with the abundance of the matrix polysaccharide VPS, which connects the local molecular composition of the biofilm to the microscopic cell tracks and mesoscopic material property of the cellular community. Our observation of spatially-varying material properties at the cellular scale is complementary to the previous macroscopic characterizations of biofilm rheology without spatial resolution.[20,26,30–32]

The method we developed for inferring the internal elastic properties of bacterial biofilms in vivo, based on combining experimental cell tracking data and a general spring network model can be used to infer the internal properties of any inhomogeneous elastic biomaterial for which imaging with cellular resolution can be performed. As the recent improvements in 3D live-cell microscopy[52,58–61] and neural-network-based image analysis[56,62] enable single-cell-level data to be obtained for many other biological systems, we anticipate that our inference framework will be widely applicable to the rheological analysis of biomaterials in vivo at the cellular scale.

During growth, biological tissues and microbial communities consume nutrients and produce waste products, which establishes resource gradients and locally varying microenvironments, ultimately resulting in locally varying gene expression and locally varying production of matrix components. Since these resource gradients are not expected to be constant over time, we anticipate that the material properties in biofilms are not only spatially heterogeneous, as shown in this study, but also temporally heterogeneous. The full spectrum of spatiotemporal material properties of biofilms has yet to be characterized, which could reveal windows of opportunity for removing biofilms by mechanical shear, and for designing living materials with tunable shear response.

4. Experimental Section

Bacterial Cultivation and Biofilm Growth: All bacterial strains used in this study are listed in Table S1 (Supporting Information). The primary strain used in this study was derived from the *V. cholerae* N16961 wild type, by introducing the *vpvC*^{W240R} allele conferring rugosity, and by introducing the Δ*crvA* (VCA1075) mutation that results in a straight, rod-like cell shape. The strain also harbors a plasmid (pNUT542) carrying a gentamicin resistance and a P_{tac} promoter without *lacO* to drive the constitutive production of sfGFP. The resulting bacterial strain is termed KDV613,[52] and was used for all shear flow deformation experiments in this study. The other strains that were used in this study are derivatives of KDV613, with the exception of KDV2013 which harbors a different plasmid. *V. cholerae* biofilms were grown in M9 minimal medium, supplemented with 2 mM $MgSO_4$, 100 µM $CaCl_2$, MEM vitamins (Sigma), 0.5% w/v glucose, and 15 mM triethanolamine (pH 7.1). LB medium was used for overnight cultures and contained 10 g L^{-1} tryptone, 5 g L^{-1} yeast extract, and 10 g L^{-1} NaCl. Furthermore, 30 µg mL^{-1} gentamicin was added to LB and M9 media, to maintain the plasmid pNUT542.

Biofilms of *V. cholerae* producing sfGFP were grown in microfluidic flow chambers (chamber dimensions: [width; height; length] = [500; 70; 7000] µm). Flow chambers were constructed from poly(dimethylsiloxane) bonded to glass coverslips using oxygen plasma. The microfluidic design included four independent channels on each coverslip. The manufacturing process for these microfluidic channels guarantees highly reproducible channel dimensions and surface properties. Each channel was inoculated with a culture of the *V. cholerae* strain, which was prepared as follows: Cultures were grown overnight at 28 °C in liquid LB medium under shaking conditions, back-diluted 1:200 in LB medium in the morning, and grown to an optical density at 600 nm of 0.5. This culture was used for inoculating the flow channels. After inoculation of the channels, the flow was not initiated for 1 h, to allow for robust surface attachment of cells. Then, liquid M9 medium was pushed through the channel at a flow rate of 100 µL min^{-1} for 45 s, to wash away nonadherent cells and to remove LB growth medium from the channels. The flow rate through the channel was then set to 0.5 µL min^{-1}, to continuously supply fresh M9 medium into the channel for growth of the surface-adherent single cells into biofilms. Flow rates after channel inoculation and during biofilm growth were controlled using a high-precision syringe pump (Pico Plus, Harvard Apparatus).

Experiments with Varying Fluid Shear: *V. cholerae* biofilms were grown in a microfluidic flow chamber in the presence of a low flow rate (0.5 µL min^{-1}, $\dot{\gamma} \cong 20.4$ s^{-1}), which was controlled using a syringe pump. After the height of the biofilm R_z reached around 10–30 µm, the syringe pump was disconnected from the inlet to the flow chamber, and replaced by a microfluidic pressure controller (OB1 MK3+, Elveflow). The pressure controller can apply higher and more stable flow rates to the microchannel by integrating feedback from a flow sensor (MFS5, Elveflow). The flow rate, microscope stage, and 3D confocal imaging were controlled simultaneously by using MATLAB to control µManager[63] and the flow control software (ESI, Elveflow). To inhibit protein production and cell division during the experiments with strong flow, two antibiotics (10 µg mL^{-1} trimethoprim, 3 µg mL^{-1} tetracycline) were added to the M9 media and flowed through the channel for 10 min prior to starting imaging and varying the flow rates. The strong flow was applied as a step function: It started from 0 µL min^{-1}, then changed to the targeted strong flow rate, and then set to 0 µL min^{-1} again. Due to a limitation in flow rate acceleration by the pressure controller, it took 15 s to increase and stabilize the flow rate in the microfluidic channel from 0 to 2000 µL min^{-1}, which was the largest achievable amplitude in the system. Similarly, it took 15 s to decrease and stabilize the flow rate back to 0 µL min^{-1}. Imaging of 3D biofilm volumes was performed at 3 time points: before applying the strong flow, during the strong flow (1 min after the increase in flow), and 1 min after decreasing the flow rate (Figure 1A). As experimental parameters, biofilms were exposed to a different maximum flow rate (100, 200, 500, 1000, 2000 µL min^{-1}), or biofilms of different volume V (519 µm^3 < V < 6032 µm^3) were used, or the duration of the high flow rate (3, 5, 10, 20, 40 min) was varied. Each biofilm deformation measurement was performed with a previously unexposed biofilm in a different microfluidic channel.

Microscopy of Biofilms: 3D biofilms in microfluidic channels were imaged using spinning disk confocal microscopy with a 50 µm pinhole disk (Yokogawa CSU W1) mounted on a Nikon Ti-E inverted microscope, using an Olympus 100× silicone oil immersion (refractive index = 1.406) objective with NA 1.35 (N5203100). By using this silicon oil objective, distortions at *z*-positions > 10 µm into the biofilm are reduced. Fluorescence of the super-folder GFP was excited using a 488 nm laser (OBIS, Coherent), and the emitted light was filtered with a 525/50 bandpass filter. For visualization of matrix components, the fluorescent dyes were excited with a 640 nm laser (OBIS, Coherent) and the emitted light was filtered with a 731/137 bandpass filter. The fluorescent protein mRuby3 was excited with a 552 nm laser (OBIS, Coherent) and the emitted light was filtered with a 650/150 bandpass filter. Images were acquired with an Andor iXon Ultra 888 electron-multiplying charge-coupled device camera. Images were acquired with a magnification of 63.2 nm per pixel in the *xy*-plane and 100 nm spacing in the *z*-direction for all experiments. Very low excitation light intensities and 90 ms exposure times were used for all experiments to reduce photodamage as much as possible. Focus drift was prevented using a Nikon hardware autofocus system.

Flow Profile in the Channel and Around the Biofilm: The flow profile and shear rate along the *z*-axis in the flow channel can be estimated based on fluid mechanics theory. The geometry of the channel and the *xyz*-coordinate system used below are illustrated in Figure S2A (Supporting Information). The relevant geometric parameters of the flow channel are the height $h_c = 70$ µm and width $w_c = 500$ µm. At the maximum flow rate that was used in the experiments, $Q = 2000$ µL min^{-1}, the maximum Reynolds number of the flow is defined as $Re_{max} = uL/\upsilon = u_{average}\, D_h/\upsilon = 131$, with the averaged flow speed $u_{average} = 0.952$ m s^{-1}, the hydraulic diameter $D_h = 4A_c/p_c = 4h_cw_c/(2h_c + 2w_c) = 123$ µm (A_c: the cross-sectional flow area, p_c: the wetted perimeter), and the kinetic viscosity of water $\upsilon = 0.893$ mm^2 s^{-1} at 25 °C. In the system, the maximum Reynolds number is still significantly smaller than Reynolds numbers for which turbulent flows are observed ($Re > 10^3$). Therefore, laminar flow was assumed for the system, which is consistent with all experimental flow visualizations that were performed (see Video S2, Supporting Information). In laminar flow, the parabolic flow profile in the channel in the *x*-direction as a function of *z* is

$$u_x(z) = 4u_{max}\frac{z}{h_c}\left(1 - \frac{z}{h_c}\right) \quad (1)$$

which can be used in the center of the channel along the *y*-axis.[64] Here, $u_{max} = 3Q/2h_cw_c$ is the maximum flow speed within the channel and Q is the flow rate.

The shear rate at the bottom of the channel ($z = 0$) without biofilms is $\dot{\gamma} = u'(z)|_{z=0} = 6Q/{h_c}^2w_c$. The flow rate, which is the parameter that was set experimentally, is linearly proportional to the shear rate, and a conversion is provided for the experimentally relevant parameter values in Figure S2G (Supporting Information). At the flow rate $Q = 2000$ µL min^{-1}, $u_{max} = 1.43$ m s^{-1}, and $\dot{\gamma} = 8.16 \times 10^4$ s^{-1} are obtained. To estimate the shear stress on the wall of the microchannel, the Darcy friction factor[65] as $f = 80.8/Re = 0.617$ was used. Using the maximum flow rate $Q = 2000$ µL min^{-1}, and the density of water $\rho = 997$ kg m^{-3} at 25 °C, the maximum shear stress on the wall of the surface is $\tau_{max} = f\rho{u_{average}}^2/8 = 69.7$ N m^{-2}.

For measuring the flow field around a biofilm in the channel, biofilms were grown as described above, and just before imaging, fluorescent beads (FluoSpheres 0.1 µm, F8803, Thermo Fisher) were added at a 1:1000 dilution as flow tracer particles to the M9 medium that flowed through the channel at 1 µL min^{-1}. Fluorescence of flowing beads was excited using a 552 nm laser and confocal *xy*-images were acquired with an exposure time of 15 ms (Figure S2B, Supporting Information). To obtain large field of view that encompasses the entire biofilm colony in each *xy*-plane, a Nikon 40× oil immersion objective with NA 1.3 (MRH01401) was used. Without the flow (i.e., if the flow rate was set to 0 µL min^{-1}), the beads in the image are detected as circles. With the flow, the beads in the image travel appear elongated along the flow lines. The length of an "elongated bead" represents the distance which the bead traveled during the exposure time, which provides a convenient basis for computing flow field vectors. To measure the flow field in 3D around the biofilm, a *z*-stack with a *z*-spacing of 1 µm was acquired. For each *z*-slice a single image in the fluorescence channel of the biofilm was acquired and 1000 image frames in the fluorescence channel of the beads were acquired. Using these data, binned flow field vectors and the location of the biofilm were obtained for every *z*-slice (Figure S2C, Supporting Information). These measurements showed that the flow speed far from a biofilm is nearly constant in the *x*- and *y*-direction (Figure S2D, Supporting Information). As a control experiment, the flow field was also measured in the *y*-middle of the channel as a function of *z* without biofilms (Figure S2F, Supporting Information). These measurements showed that the flow speed close to the top and bottom surfaces of the channel were not measured correctly, but for measurements that are >5 µm away from the surfaces, the flow profile along the *z*-axis is parabolic (Figure S2F, Supporting Information), which is consistent with theoretical expectations for a channel without biofilms (Figure S2E, Supporting Information). In addition, the measured maximum flow velocity corresponded to the theoretical maximum flow velocity: $u_{max} = 714$ µm s^{-1} at a flow rate of $Q = 1$ µL min^{-1}.

Visualization of Matrix Components of V. Cholerae Biofilms: Four bacterial strains were used to visualize four different biofilm matrix components of *V. cholerae* (see Table S1 of a list of all strains, Supporting Information). Strain KDV1663 was used to visualize RbmA, based on replacing the original copy of *rbmA* on the chromosome version that encodes a His-tag. Strain KDV1625 was used to visualize Bap1, based on replacing the original copy of *bap1* on the chromosome with a version that encodes a FLAG-tag. Strain KDV1491 was used to visualize RbmC, based on replacing the original copy of *rbmC* on the chromosome with a version that encodes a FLAG-tag. Strains KDV1663, KDV1625, and KDV1491 were developed previously[46] and are derivatives of the strain KDV613, with which the biofilm deformation experiments were performed in this study. Strain KDV2013 was used to visualize VPS production based on staining VPS with lectins that are conjugated to green fluorescent dyes. Strain KDV2013 is identical to KDV613, except that this strain does not harbor the plasmid pNUT542 that results in the production of the green-fluorescent protein sfGFP, but instead harbors the plasmid pNUT1029 that results in the constitutive production of the red-fluorescent protein mRuby3.

For imaging the localization and abundance of biofilm matrix components, the relevant strains were grown separately in microfluidic flow chambers with a flow rate of 0.5 µL min^{-1} M9 media, as described above. The microscopy settings were as described above for single-cell-level imaging, with the exception that a *z*-spacing of 400 nm was used, and that one additional fluorescent channel for imaging the matrix components was used. For imaging of RbmA-His, 1 µg mL^{-1} of Penta His Alexa Fluor 647 (Thermo Scientific) and 1 mg mL^{-1} of filter-sterilized bovine serum albumin (BSA) were added into M9 media 15 min before imaging. For imaging of Bap1-FLAG, 1 µg mL^{-1} of DYKDDDK tag monoclonal antibody Alexa Fluor 647 (Thermo Scientific) and 1 mg mL^{-1} of filter-sterilized BSA were added into M9 media 15 min before imaging. For imaging of RbmC-FLAG, 1 µg mL^{-1} of DYKDDDK tag monoclonal antibody Alexa Fluor 647 (Thermo Scientific) and 1 mg mL^{-1} of filter-sterilized BSA were added into M9 media 15 min before imaging. For imaging of VPS, 20 µg mL^{-1} of wheat-germ agglutinin (WGA) Alexa Fluor 647 (Thermo Scientific), 20 µg mL^{-1} Concanavalin A Alexa Fluor 633 (Thermo Scientific), and 1 mg mL^{-1} of filter-sterilized BSA were added into M9 media 30 min before imaging. Then, immediately prior to imaging, this fluorescent lectin-containing liquid was flushed out to reduce background fluorescence. To quantify biofilm-internal spatial distributions of the matrix components, BiofilmQ was used.[54]

Testing Resilience of Biofilms Formed by V. Cholerae Mutants to High Shear Rates: The above methods were used for biofilm growth and microscopy to determine the responses of *V. cholerae* mutants to strong shear flow. The following strains were tested: wild type (KDV613), Δ*rbmC* mutant (KDV1412), Δ*bap1* mutant (KDV1414), Δ*rbmA* mutant (KDV692), and Δ*vpsL* mutant (KDV1890), as listed in Table S1 (Supporting Information). Before applying the strong fluid shear rate, 3D volume images of biofilms were acquired at a flow rate of 0 µL min^{-1}. Then the flow rate was increased to 10, 100, 200, 500, 1000, 2000, and 4000 µL min^{-1}, for 1 min to each flow

rate. A flow rate of 4000 µL min^{-1} corresponds to a shear rate of $\dot{\gamma} = 1.63 \times 10^5\ s^{-1}$. After applying the shear rate of $\dot{\gamma} = 1.63 \times 10^5\ s^{-1}$ for 1 min, the flow was stopped to 0 µL min^{-1} and another set of 3D volume images of the biofilms were acquired, shown in Figure S13 (Supporting Information).

Single-Cell Segmentation and Analysis: For 3D segmentation of all individual cells in biofilm images, a trained model of StarDist OPP, which is a cell segmentation algorithm based on a convolutional neural network (CNN), was used.[53] The StarDist OPP model was trained with a dataset involving 3D slices of *V. cholerae* biofilms imaged by the microscope system. By using StarDist OPP, the accuracy of cell segmentation for 3D bacterial biofilm volume image is above 80%, which is higher than any other single-cell segmentation method achieved on the biofilm image data. To calculate single-cell parameters and whole-biofilm parameters from the single-cell segmentation labels, the BiofilmQ software was used.[54]

Single-Cell Tracking in Biofilms with Large Cellular Displacements: Cell tracking between the 3 different time points (before, during, and after strong shear flow) was performed with an iterative algorithm, which is based on the following observations: First, it was noticed that during shear-flow induced biofilm deformation and during biofilm relaxation after shear-flow reduction, the relative positions of cells in the biofilm are not changed. Second, the cells at the base surface display only a very small displacement during strong shear flow, which makes these cells easy to track. Third, the magnitude of cell displacements gradually increases with increasing the *z*-positions, analogous to the increase of fluid shear toward the center of the flow chamber.

Based on the above observations, cells were tracked by iteratively identifying temporal connections between cells, starting with the bottom-most cells that display only small displacements, and gradually considering cells with higher *z*-coordinates as described in Figure S1 (Supporting Information). This algorithm is based on several distinct steps, as shown in Figure S1 (Supporting Information). In step 1 of this algorithm, the three 3D biofilm images of the time series were segmented using the trained CNN model that is part of the StarDist OPP algorithm.[53] This segmentation results in a labeled object for each individual cell. In step 2 of the algorithm, one cell at the bottom surface of the biofilm is tracked manually. This is achieved by manually comparing the bottom view of 3D renderings of biofilms between two successive time points. Here, humans can easily track at least one cell across time. In step 3 of the algorithm, a displacement vector from the trajectory of the tracked cell was computed, to estimate predicted positions of the surrounding cells in the next time frame. Then, the overlap volume between the predicted cell positions and actual cells in the next frame is computed. When the predicted cell position has a large overlap with an actual cell, this cell is determined as the tracked cell. When the predicted cell is overlapping with more than one or no cells, the cell is not considered to be tracked to avoid uncertain tracking results. Through this process, many cells surrounding the initial (manually tracked) cell can be tracked. By iteration of step 3, the tracking propagates from the center of the bottom surface of the biofilm to the outer biofilm surface (Figure S1, step 3 bottom, Supporting Information). However, the number of tracks eventually saturates due to the above self-validation that leads to the exclusion of uncertain tracks. After the tracking saturation in the step 3, step 4 was performed, which uses the strain field of biofilm deformation to track more cells across the 3 time points. To obtain the required strain field measurements, 3D quasiconformal maps, as described in the section below, were used. Based on the 3D quasiconformal mapping results, the overlap volume between the mapped positions of cells and the actual position of cells was computed, and strongly overlapping cells as tracks were connected, which further improved the tracking results, particularly for cells with larger displacements.

Strain Measurements Using 3D Quasiconformal Maps: 3D quasiconformal maps were used to extract the strain field of the biofilm in shear flow. In complex analysis, conformal maps are functions on the complex plane that locally preserve angles. Intuitively, under a conformal map, a packing of small circles on a planar domain on the complex plane will be mapped to another packing of small circles in which the circles may change in size and orientation but not aspect ratio. Quasiconformal maps are a generalization of conformal maps that map small circles to small ellipses with bounded eccentricity.[66] It is natural to consider the 3D analogue of quasiconformal maps, which take a packing of small spheres to a packing of small ellipsoids. To extend the computation of quasiconformal maps for 3D domains, a possible approach[67] is to define the quasiconformal distortion K_f of a 3D quasiconformal map f: $\Omega \to \Omega$ by

$$K_f(X) = \frac{\beta_1(X) + \beta_2(X) + \beta_3(X)}{3\left(\beta_1(X)\,\beta_2(X)\,\beta_3(X)\right)^{\frac{1}{3}}} \tag{2}$$

where $\Omega \subset R^3$ is a domain containing the biofilm, $\beta_1(X), \beta_2(X), \beta_3(X)$ are the eigenvalues of $(Df)^T(Df)$, Df is the Jacobian matrix of f, and $X = (x, y, z)$ is a point in the domain (i.e., within the biofilm). Note that by the inequality of arithmetic means and geometric means,

$$\frac{\beta_1(X) + \beta_2(X) + \beta_3(X)}{3} \geq \left(\beta_1(X)\,\beta_2(X)\,\beta_3(X)\right)^{\frac{1}{3}} \tag{3}$$

and hence $K_f \geq 1$. The equality holds if, and only if, $\beta_1 = \beta_2 = \beta_3$, i.e., f is conformal.

Now, given a biofilm at two different time points i, j and a set of tracked cell center positions $\{\boldsymbol{r}_{i,k}\}_{k=1}^{N} \leftrightarrow \{\boldsymbol{r}_{j,k}\}_{k=1}^{N}$ within the biofilm (where N is the total number of tracked pairs, $\boldsymbol{r}_{i,k}$ is the kth tracked cell center position at the time point i, and $\boldsymbol{r}_{j,k}$ is the corresponding kth tracked cell center position at the time point j), a smooth 3D quasiconformal map f between the two time points that matches the tracked cell positions (i.e., with $f(\boldsymbol{r}_{i,k}) = \boldsymbol{r}_{j,k}$ for all $k = 1, 2, \ldots, N$) and minimizes the quasiconformal distortion $\|K_f\|_1$ was computed.

Using the map f, the strain components can be extracted to analyze the local geometric distortion of the biofilm under the shear flow. More specifically, by expressing f as $f(x, y, z) = (f_1(x,y,z), f_2(x,y,z), f_3(x,y,z))$, the displacements of every point in *x*-, *y*-, and *z*-directions (denoted by $d_1(x,y,z)$, $d_2(x,y,z)$, and $d_3(x,y,z)$, respectively) under f are given by

$$d_1(x, y, z) = f_1(x, y, z) - x \tag{4}$$

$$d_2(x, y, z) = f_2(x, y, z) - y \tag{5}$$

$$d_3(x, y, z) = f_3(x, y, z) - z \tag{6}$$

The strain components are then given by

$$\epsilon_{xx} = (d_1)_x,\ \epsilon_{yy} = (d_2)_y,\ \epsilon_{zz} = (d_3)_z \tag{7}$$

$$\epsilon_{xy} = \frac{1}{2}\left((d_1)_y + (d_2)_x\right),\ \epsilon_{xz} = \frac{1}{2}\left((d_1)_z + (d_3)_x\right),\ \epsilon_{yz} = \frac{1}{2}\left((d_2)_z + (d_3)_y\right) \tag{8}$$

Multiple-Spring Model to Describe Stiffness of Cell–Cell Binding: Inference of mechanical properties: Using observations of tracked cells before and during biofilm deformation, the mechanical properties of a biofilm are inferred. In general, to perform mechanical inference from observations of a system, a mathematical model for the mechanics of that system is required. This model will have some unknown parameters which one then needs to infer. Typically, there are many parameter values consistent with the observations, so the inverse problem is solved by using some form of regularization.[68] Here, the mechanical structure of the biofilm is modeled as a spring network with unknown spring stiffnesses (Figure 4A), and regularized by searching for solutions which have locally continuous mechanical properties.

The model for the mechanics is a general spring network, which can approximate any inhomogeneous elastic material. Given data of tracked cell centroids, the cell centroids, $\{\boldsymbol{r}_i\}$, were taken as vertex locations and connected with springs of unknown stiffness. Vertices i and j that are neighbors in the Delaunay tessellation, the dual of the Voronoi diagram, are connected by an edge $e = (i, j)$ representing a spring. Assuming linear

springs (infinitesimal deformations are not assumed) the elastic energy of the system is

$$H = \sum_e k_e \left(l_e - l_e^0\right)^2 \tag{9}$$

where $l_e = l_e\,(\boldsymbol{r}_i, \boldsymbol{r}_j)$ is the current length of spring e, l_e^0 the rest length of this spring, and k_e is the spring stiffness. Assuming that there are no internal forces in the system at $t = 0$, each spring is taken to be at rest length, and hence l_e^0 is deduced.

The system is then considered while flow is being applied. The system is held out of the rest state, so $l_e \neq l_e^0$ in general. Now, a distinction is made between external vertices on the biofilm boundary which feel external forces, and vertices in the biofilm interior which only feel the elastic forces from other vertices. How to classify whether cells belong to the biofilm interior or to the biofilm boundary is discussed in the next section. For a steady flow, as used in the experiments, forces acting on any vertex must balance. For external vertices (those on the boundary of the biofilm) this includes some unknown force due to the flow (for cells on the fluid-facing biofilm boundary) or adhesive interaction with the substrate surface (for cells on the substrate-surface-facing biofilm boundary), and hence their force-balance equation is not considered. Even without knowing the forces acting on these external vertices, it is possible to deduce the internal elastic properties of the biofilm.

For biofilm-internal vertices, the elastic forces balance. Thus, for some internal vertex i,

$$\frac{\partial H}{\partial \boldsymbol{r}_i} = \sum_{e=(i,j)} k_e \frac{\partial l_e}{\partial \boldsymbol{r}_i}\left(l_e - l_e^0\right) = 0 \tag{10}$$

where the sum is taken over all edges connected to i, including ones connected to external vertices that are part of the biofilm boundary. Define $\vec{q}$ to be a vector with components $q_e = k_e\,(l_e - l_e^0)$, representing the force within each spring, for springs connected to at least one internal vertex, and define E to be the length of this vector. It then follows that

$$A\,\vec{q} = 0 \tag{11}$$

where A is the $3M \times E$ matrix of constraints, where M is the number of internal vertices. It is expected that $E > 3M$, so in general there are many such solutions for $\vec{q}$, where finding $\vec{q}$ and finding k_e are equivalent since the spring lengths are known. Therefore, a regularization rule must be introduced,[68] guided by physical intuition, to infer $\vec{q}$.

The combination $l_e^0 k_e$, rather than k_e alone, is analogous to a continuum elastic modulus, and is regularized by searching for solutions which vary continuously across the material. Specifically, take

$$k \circ l^0 = \sum_{i=1}^{n} b_i\,\vec{\phi}_i = \Phi b \tag{12}$$

where $\vec{\phi}_i$ are the eigenvectors of the Laplacian L, and $k \bigcirc l^0$ is a vector with components $k_e l_e^0$. By only taking a small number of eigenvectors, one can restrict the variation of elastic properties to low wavelength modes. If n is small enough, one cannot satisfy

$$A\left[\left(\frac{l}{l^0} - 1\right) \circ (\Phi b)\right] = 0 = Tb \tag{13}$$

exactly, where this equation defines the matrix T. Instead, one should minimize $\|Tb\|_2$ subject to k_e being positive and $\|b\|_2 = 1$, the choice of unit norm meaning that b is only found up to an overall scaling. In finding such a minimum, the problem has been regularized, allowing a particular solution for the material properties to be inferred, at least up to an overall scaling constant.

Identification of Cells that are Part of the Biofilm Boundary or Biofilm Interior: For experimental biofilms, any tracked cells which lie on the surface but are not part of the main biofilm colony were removed. This is done by projecting all cell centroids onto the surface, $(x, y, z) \mapsto (x, y, 0)$, computing a cell number density round each cell, and removing cells with a density below a threshold. Specifically, density is computed with a kernel density estimate using an exponential kernel with bandwidth $\sigma = 3$ µm, so that

$$\rho_{\text{kernel}}\,(\vec{\mathbf{r}}) = \sum_i \exp\left[-\frac{\|\boldsymbol{r}_i - \vec{\mathbf{r}}\|_2}{\sigma}\right] \tag{14}$$

and cells with a density less than 100.0 were removed, which typically removes fewer than 5% of cells. Once these cells are removed, they are not used elsewhere in the analysis. These cells are attached directly to the substrate surface, not to cells in the main biofilm colony and hence their displacements are not informative for inferring biofilm-internal elastic properties.

Next, external vertices (cells on the boundary of the biofilm) were identified using an alpha-shape[69] of radius 4 µm. In short, if a sphere of radius 4 µm can touch a particular cell centroid without enclosing any other cell centroids, then that centroid is considered to be a cell on the biofilm boundary, otherwise it is considered to be an internal cell. These external vertices have an unknown force balance; they interact both with internal elastic forces as well as external forces like fluid shear and surface adhesion.

Testing the Inference Framework: The robustness of the inference framework is demonstrated by showing that it can recover back spring stiffness (k_e), and moduli ($l_e^0 k_e$). To incorporate realistic cell–cell spacing and cell deformations into this test, an experimental biofilm was used, before and during flow, as the basis for a simulation. For a biofilm before flow, the centroids of cells in the biofilm interior were taken as vertices and those vertices were connected with springs if they were neighbors in the Delaunay tessellation. In this test simulation, in principle any spring stiffness can be prescribed. For the time point during flow, the positions of the vertices that belong to the biofilm boundary were taken as fixed (they were identified as outlined in the previous section) and then the elastic energy, H, was minimized with respect to the position of the biofilm-internal vertices. The final position of the biofilm-internal vertices after minimization will not, in general, match the experimental positions, and will depend on the choice of spring stiffnesses.

The inverse procedure of the inference framework, described above, should be able to robustly recover the spring stiffnesses from this simulated deformation because the simulation, by construction, is consistent with the spring network model. While an exact reconstruction is not expected due to the regularization, for spring moduli linearly decreasing with biofilm radius it is found that there is an almost perfect reconstruction of stiffness (k_e) and a recovery of the linear gradient in $l_e^0 k_e$, as shown in Figure S10A (Supporting Information). Perturbing the true stiffnesses by $k_e \mapsto k_e \times (1 + \delta)$, where δ is a uniform random variable $\delta \sim$ Uniform[−0.05, 0.05], still results in a good reconstruction (Figure S10B, Supporting Information), even though this perturbation results in a k_e that is not consistent with the assumption that $l_e^0 k_e$ is spatially continuous. Note that the overall scaling of the inferred k_e is still arbitrary, and in Figure S10 (Supporting Information) it was scaled to match the exact values. This scaling cannot be determined from deformations alone, how it may be inferred is described below.

Inference From Experimental Data: For inferring the spatial distribution of spring stiffnesses in biofilms, large biofilms (volume >2600 µm^3) which were exposed to the step-up in flow rate from 0 to 2000 µL min^{-1} were used, for which there are 10 independent replicate experiments on different biofilms. For each of these experiments, the same procedure described in detail above, and outlined briefly again here was performed: First, cells on the substrate which are not part of the biofilm were removed by density thresholding, then cells that belong to the biofilm-interior and biofilm-boundary were identified with an alpha-shape of radius $\alpha = 4$ µm. Finally, spring stiffnesses was inferred using $n = 50$ Laplace modes (Figure S14, Supporting Information).

To identify systematic spatial trends in the elastic properties of biofilms, data was used from 10 independent replicate experiments, in order to reduce the effect of variability of different biofilms. However, the inference framework determines the stiffnesses only up to an arbitrary scaling. In order to combine different biofilms, a scaling was applied so that the median spring stiffness for each biofilm is equal. Next, each inferred stiffness was associated to the spatial midpoint of the corresponding spring, and then the coordinates were rescaled to make all biofilms the same size, $(x, y, z) \mapsto (x/R_{xy}, y/R_{xy}, z/R_z)$. After performing these transformations, the data of biofilms from different experiments can be combined, in order to compute the relative moduli at each relative coordinate. This analysis shows that biofilms are stiffest in their core (Figure 4B).

The spring modulus $l_e^0 k_e$ was only determined up to an overall scaling constant. In principle, this global scaling constant could be estimated from knowledge of the force exerted by the fluid flow. For instance, a hemisphere of radius a in a linear Stokes flow of flow rate $\dot{\gamma}$, experiences a total force exerted on it in the direction of flow of $4.3\pi a^2 \dot{\gamma} \mu$, where μ is the viscosity of the fluid.[70] For the vertices that belong to the biofilm boundary, the total force exerted on them by the internal vertices, which is known, must balance with the force exerted on them by the flow. Assuming the biofilm shape is a hemisphere, this could be used to find the global scaling. However, the biofilm shape is not exactly hemispherical and differs between biofilms. While such an argument could be used to find an order of magnitude estimate for the scaling, it is not used for the inference. Instead, conclusions were only drawn about relative stiffness within the biofilms.

The elastic modulus inference can only be performed for the biofilm-internal region, and not for the region that includes the cells which are directly attached to the substrate surface (this region is shown in gray in Figure 4B). The height of this region is the average cell–cell distance 0.694 µm divided by the average biofilm height 15.3 µm, i.e., $0 \leq z/R_z \leq 0.0453$.

Supporting Information

Supporting Information is available from the Wiley Online Library or from the author.

Acknowledgements

The authors are grateful to Eric Jelli and Niklas Netter for helping training the CNN model in StarDist OPP, which was used for performing the single-cell segmentation of biofilm images. This study was enabled by a grant from the European Union's Horizon 2020 research and innovation program through the European Research Council (716734 to K.D.), a Swiss National Science Foundation Consolidator Grant (TMCG-3_213801 to K.D.), a grant from the Deutsche Forschungsgemeinschaft (DR 982/6-1 to K.D.) as part of the Priority Programme SPP 2389, a grant from the Minna James Heineman Foundation (to K.D.), and by the National Center of Competence in Research AntiResist funded by the Swiss National Science Foundation (Grant No. 51NF40_180541, to K.D.). In addition, this work was supported by a Cross-Disciplinary Fellowship of the Human Frontier Science Program Organization (LT000013/2019-C to T.O.), a fellowship from the Japan Society for the Promotion of Science (17J10331 to T.O.), as well as a MathWorks Science Fellowship (to D.J.S.), National Science Foundation Award DMS-1764421 (to D.J.S.), and DMS-2002103 (to G.P.T.C.), Simons Foundation grant 597491 (to D.J.S.), National Science Foundation Award DMR-2214021 (to J.D.), the MIT Mathematics Robert E. Collins Distinguished Scholar Fund (to J.D.), the MIT MathWorks Professorship (to J.D), and the Sloan Foundation Grant G-2021-16758 (to J.D.). This project is supported by Schmidt Sciences (Polymath Award to J.D.).

Conflict of Interest

The authors declare no conflict of interest.

Author Contributions

T.O., J.D., and K.D. designed the research; T.O. and K.N. performed the experiments; T.O. performed the image analysis; T.O. and G.P.T.C. analyzed the data extracted from images; D.S. and J.D. developed the theoretical model and performed analyses with this model; T.O. and K.D. wrote the manuscript with the input of all authors; J.D. and K.D. supervised the project.

Data Availability Statement

The data that support the findings of this study are openly available in Zenodo at https://doi.org/10.5281/zenodo.10091010, reference number 10091010.

Keywords

biofilm, extracellular matrix, force inference, rheology, shear flow, single-cell tracking

Received: December 22, 2023
Revised: March 8, 2024
Published online:

[1] H. C. Flemming, S. Wuertz, *Nat. Rev. Microbiol.* **2019**, *17*, 247.
[2] C. R. Arciola, D. Campoccia, L. Montanaro, *Nat. Rev. Microbiol.* **2018**, *16*, 397.
[3] H. Koo, R. N. Allan, R. P. Howlin, P. Stoodley, L. Hall-Stoodley, *Nat. Rev. Microbiol.* **2017**, *15*, 740.
[4] D. Lebeaux, J.-M. Ghigo, C. Beloin, *Microbiol. Mol. Biol. Rev.* **2014**, *78*, 510.
[5] H. C. Flemming, E. D. van Hullebusch, T. R. Neu, P. H. Nielsen, T. Seviour, P. Stoodley, J. Wingender, S. Wuertz, *Nat. Rev. Microbiol.* **2023**, *21*, 70.
[6] H. Kim, D. J. Skinner, D. S. Glass, A. E. Hamby, B. A. R. Stuart, J. Dunkel, I. H. Riedel-Kruse, *Nature* **2022**, *608*, 324.
[7] A. Persat, C. D. Nadell, M. K. Kim, F. Ingremeau, A. Siryaporn, K. Drescher, N. S. Wingreen, B. L. Bassler, Z. Gitai, H. A. Stone, *Cell* **2015**, *161*, 988.
[8] A. Cubillos-Ruiz, T. Guo, A. Sokolovska, P. F. Miller, J. J. Collins, T. K. Lu, J. M. Lora, *Nat. Rev. Drug Discovery* **2021**, *20*, 941.
[9] S. Galié, C. García-Gutiérrez, E. M. Miguélez, C. J. Villar, F. Lombó, *Front. Microbiol.* **2018**, *9*, 898.
[10] C. E. Lawson, W. R. Harcombe, R. Hatzenpichler, S. R. Lindemann, F. E. Löffler, M. A. O'Malley, H. García Martín, B. F. Pfleger, L. Raskin, O. S. Venturelli, D. G. Weissbrodt, D. R. Noguera, K. D. McMahon, *Nat. Rev. Microbiol.* **2019**, *17*, 725.
[11] Y. Cao, M. C. M. van Loosdrecht, G. T. Daigger, *Appl. Microbiol. Biotechnol.* **2017**, *101*, 1365.
[12] J. K. Teschler, D. Zamorano-Sánchez, A. S. Utada, C. J. A. Warner, G. C. L. Wong, R. G. Linington, F. H. Yildiz, *Nat. Rev. Microbiol.* **2015**, *13*, 255.
[13] J. K. Teschler, C. D. Nadell, K. Drescher, F. H. Yildiz, *Annu. Rev. Microbiol.* **2022**, *76*, 503.
[14] L. Karygianni, Z. Ren, H. Koo, T. Thurnheer, *Trends Microbiol.* **2020**, *28*, 668.
[15] L. Hobley, C. Harkins, C. E. MacPhee, N. R. Stanley-Wall, *FEMS Microbiol. Rev.* **2015**, *39*, 649.
[16] N. Billings, A. Birjiniuk, T. S. Samad, P. S. Doyle, K. Ribbeck, *Rep. Prog. Phys.* **2015**, *78*, 036601.
[17] M. Tallawi, M. Opitz, O. Lieleg, *Biomater. Sci.* **2017**, *5*, 887.

[18] P. Stoodley, Z. Lewandowski, J. D. Boyle, H. M. Lappin-Scott, *Biotechnol. Bioeng.* **1999**, *65*, 83.
[19] J. D. Mathias, P. Stoodley, *Biofouling* **2009**, *25*, 695.
[20] M. Jafari, P. Desmond, M. C. M. van Loosdrecht, N. Derlon, E. Morgenroth, C. Picioreanu, *Water Res.* **2018**, *145*, 375.
[21] P. Stoodley, R. Cargo, C. J. Rupp, S. Wilson, I. Klapper, *J. Ind. Microbiol. Biotechnol.* **2002**, *29*, 361.
[22] B. W. Peterson, Y. He, Y. Ren, A. Zerdoum, M. R. Libera, P. K. Sharma, A. J. van Winkelhoff, D. Neut, P. Stoodley, H. C. van der Mei, H. J. Busscher, *FEMS Microbiol. Rev.* **2015**, *39*, 234.
[23] H. Boudarel, J.-D. Mathias, B. Blaysat, M. Grédiac, *NPJ Biofilms Microbiomes* **2018**, *4*, 17.
[24] E. S. Gloag, S. Fabbri, D. J. Wozniak, P. Stoodley, *Biofilm* **2020**, *2*, 100017.
[25] S. G. V. Charlton, M. A. White, S. Jana, L. E. Eland, P. G. Jayathilake, J. G. Burgess, J. Chen, A. Wipat, T. P. Curtis, *J. Bacteriol.* **2019**, *201*, e00101.
[26] S. Geisel, E. Secchi, J. Vermant, *Interface Focus* **2022**, *12*, 20220032.
[27] J. W. Hart, T. A. Waigh, J. R. Lu, I. S. Roberts, *Langmuir* **2019**, *35*, 3553.
[28] A. Birjiniuk, N. Billings, E. Nance, J. Hanes, K. Ribbeck, P. S. Doyle, *New J. Phys.* **2014**, *16*, 085014.
[29] E. C. Hollenbeck, C. Douarche, J. M. Allain, P. Roger, C. Regeard, L. Cegelski, G. G. Fuller, E. Raspaud, *J. Phys. Chem. B* **2016**, *120*, 6080.
[30] J. Yan, A. Moreau, S. Khodaparast, A. Perazzo, J. Feng, C. Fei, S. Mao, S. Mukherjee, A. Košmrlj, N. S. Wingreen, B. L. Bassler, H. A. Stone, *Adv. Mater.* **2018**, *30*, 1804153.
[31] S. G. V. Charlton, D. L. Kurz, S. Geisel, J. Jimenez-Martinez, E. Secchi, *Interface Focus* **2022**, *12*, 20220035.
[32] E. S. Gloag, G. K. German, P. Stoodley, D. J. Wozniak, *Sci. Rep.* **2018**, *8*, 9691.
[33] P. Pearce, B. Song, D. J. Skinner, R. Mok, R. Hartmann, P. K. Singh, H. Jeckel, J. S. Oishi, K. Drescher, J. Dunkel, *Phys. Rev. Lett.* **2019**, *123*, 258101.
[34] R. Rusconi, S. Lecuyer, L. Guglielmini, H. A. Stone, *J. R. Soc. Interface* **2010**, *7*, 1293.
[35] R. Rusconi, S. Lecuyer, N. Autrusson, L. Guglielmini, H. A. Stone, *Biophys. J.* **2011**, *100*, 1392.
[36] K. Drescher, Y. Shen, B. L. Bassler, H. A. Stone, *Proc. Natl. Acad. Sci. USA* **2013**, *110*, 4345.
[37] M. Kevin Kim, K. Drescher, O. Shun Pak, B. L. Bassler, H. A. Stone, *New J. Phys.* **2014**, *16*, 065024.
[38] E. Secchi, G. Savorana, A. Vitale, L. Eberl, R. Stocker, R. Rusconi, *Proc. Natl. Acad. Sci. USA* **2022**, *119*, e2113723119.
[39] D. L. Kurz, E. Secchi, F. J. Carrillo, I. C. Bourg, R. Stocker, J. Jimenez-Martinez, *Proc. Natl. Acad. Sci. USA* **2022**, *119*, e2122202119.
[40] P. S. Stewart, M. J. Franklin, *Nat. Rev. Microbiol.* **2008**, *6*, 199.
[41] C. W. Hall, T.-F. Mah, *FEMS Microbiol. Rev.* **2017**, *41*, 276.
[42] J. Jo, A. Price-Whelan, L. E. P. Dietrich, *Nat. Rev. Microbiol.* **2022**, *20*, 593.
[43] V. Berk, J. C. N. N. Fong, G. T. Dempsey, O. N. Develioglu, X. Zhuang, J. Liphardt, F. H. Yildiz, S. Chu, *Science* **2012**, *337*, 236.
[44] C. D. Nadell, K. Drescher, N. S. Wingreen, B. L. Bassler, *ISME J.* **2015**, *9*, 1700.
[45] L. K. Jennings, K. M. Storek, H. E. Ledvina, C. Coulon, L. S. Marmont, I. Sadovskaya, P. R. Secor, B. S. Tseng, M. Scian, A. Filloux, D. J. Wozniak, P. L. Howell, M. R. Parsek, *Proc. Natl. Acad. Sci. USA* **2015**, *112*, 11353.
[46] J. C. N. Fong, A. Rogers, A. K. Michael, N. C. Parsley, W. C. Cornell, Y. C. Lin, P. K. Singh, R. Hartmann, K. Drescher, E. Vinogradov, L. E. P. Dietrich, C. L. Partch, F. H. Yildiz, *Elife* **2017**, *6*, e26163.
[47] X. Huang, T. Nero, R. Weerasekera, K. H. Matej, A. Hinbest, Z. Jiang, R. F. Lee, L. Wu, C. Chak, J. Nijjer, I. Gibaldi, H. Yang, N. Gamble, W. Ng, S. A. Malaker, K. Sumigray, R. Olson, J. Yan, *Nat. Commun.* **2023**, *14*, 2104.
[48] M. U. Rahman, D. F. Fleming, L. Wang, K. P. Rumbaugh, V. D. Gordon, G. F. Christopher, *NPJ Biofilms Microbiomes* **2022**, *8*, 49.
[49] S. C. Chew, B. Kundukad, T. Seviour, J. R. C. Van der Maarel, L. Yang, S. A. Rice, P. Doyle, S. Kjelleberg, *mBio* **2014**, *5*, e01536.
[50] O. Galy, P. Latour-Lambert, K. Zrelli, J.-M. Ghigo, C. Beloin, N. Henry, *Biophys. J.* **2012**, *103*, 1400.
[51] K. Zrelli, O. Galy, P. Latour-Lambert, L. Kirwan, J. M. Ghigo, C. Beloin, N. Henry, *New J. Phys.* **2013**, *15*, 125026.
[52] R. Hartmann, P. K. Singh, P. Pearce, R. Mok, B. Song, F. Díaz-Pascual, J. Dunkel, K. Drescher, *Nat. Phys.* **2019**, *15*, 251.
[53] E. Jelli, T. Ohmura, N. Netter, M. Abt, E. Jiménez-Siebert, K. Neuhaus, D. K. H. Rode, C. D. Nadell, K. Drescher, *Mol. Microbiol.* **2023**, *119*, 659.
[54] R. Hartmann, H. Jeckel, E. Jelli, P. K. Singh, S. Vaidya, M. Bayer, D. K. H. H. Rode, L. Vidakovic, F. Díaz-Pascual, J. C. N. N. Fong, A. Dragoš, O. Lamprecht, J. G. Thöming, N. Netter, S. Häussler, C. D. Nadell, V. Sourjik, Á. T. Kovács, F. H. Yildiz, K. Drescher, *Nat. Microbiol.* **2021**, *6*, 151.
[55] M. Weigert, U. Schmidt, R. Haase, K. Sugawara, G. Myers, in Proc. 2020 *IEEE Winter Conf. Appl. Comput. Vis.*, IEEE, New York **2020**, 3655.
[56] E. Moen, D. Bannon, T. Kudo, W. Graf, M. Covert, D. Van Valen, *Nat. Methods* **2019**, *16*, 1233.
[57] Q. Zhang, D. Nguyen, J. B. Tai, X. Xu, J. Nijjer, X. Huang, Y. Li, J. Yan, *Adv. Funct. Mater.* **2022**, *32*, 2110699.
[58] S. Yordanov, K. Neuhaus, R. Hartmann, F. Díaz-Pascual, L. Vidakovic, P. K. Singh, K. Drescher, *Biomed. Opt. Express* **2021**, *12*, 3372.
[59] V. Voleti, K. B. Patel, W. Li, C. Perez Campos, S. Bharadwaj, H. Yu, C. Ford, M. J. Casper, R. W. Yan, W. Liang, C. Wen, K. D. Kimura, K. L. Targoff, E. M. C. Hillman, *Nat. Methods* **2019**, *16*, 1054.
[60] Y. Wan, K. McDole, P. J. Keller, *Annu. Rev. Cell Dev. Biol.* **2019**, *35*, 655.
[61] E. H. K. Stelzer, F. Strobl, B.-J. Chang, F. Preusser, S. Preibisch, K. McDole, R. Fiolka, *Nat. Rev. Methods Prim.* **2021**, *1*, 73.
[62] H. Jeckel, K. Drescher, *FEMS Microbiol. Rev.* **2021**, *45*, fuaa062.
[63] A. D. Edelstein, M. A. Tsuchida, N. Amodaj, H. Pinkard, R. D. Vale, N. Stuurman, *J. Biol. Methods* **2014**, *1*, e10.
[64] J. P. Brody, P. Yager, R. E. Goldstein, R. H. Austin, *Biophys. J.* **1996**, *71*, 3430.
[65] Y. Cengel, J. Cimbala, *Fluid Mechanics Fundamentals and Applications*, McGraw Hill, Columbus, OH **2013**.
[66] L. Ahlfors, *Lectures on Quasiconformal Mappings*, American Mathematical Society, Providence, RI **2006**.
[67] Y. T. Lee, K. C. Lam, L. M. Lui, *J. Sci. Comput.* **2016**, *67*, 926.
[68] K. K. Chiou, L. Hufnagel, B. I. Shraiman, *PLoS Comput. Biol.* **2012**, *8*, e1002512.
[69] H. Edelsbrunner, D. Kirkpatrick, R. Seidel, *IEEE Trans. Inf. Theory* **1983**, *29*, 551.
[70] T. C. Price, *Q. J. Mech. Appl. Math.* **1985**, *38*, 93.